Large-Scale Combined Adjustment of Optical Satellite Imagery and ICESat-2 Data Through Terrain Profile Elevation Sequence Similarity Matching

Shaodong Wei, Yonghua Jiang, Bin Du, MeiLin Tan, Miaozhong Xu, Weiqi Lian, and Guo Zhang, *Member, IEEE*

***Abstract*—Earth observation utilizes multisource satellite data to enhance photogrammetry mapping. This study introduces a novel method to improve the geometric positioning accuracy of large-scale optical satellite imagery by combined adjustment with NASA's Ice, Cloud, and Land Elevation Satellite-2 (ICESat-2) laser altimetry data. Although ICESat-2 is known for its high vertical accuracy, its potential to improve horizontal accuracy has been limited due to the difficulty in matching caused by temporal inconsistencies across large survey areas. To address this, our method employs a robust terrain profile elevation sequence similarity matching technique, refined with two-dimensional Gaussian fitting to achieve enhanced position extraction. We also propose a weighted adjustment strategy that uses matching confidence to enhance the precision of the combined adjustments. Large-scale tests across various terrains showed that our approach has significantly reduced horizontal and vertical positioning errors to 4.3 and 1.7 m, respectively, outperforming existing methods.**

***Index Terms*—Combined adjustment, NASA's Ice, Cloud, and Land Elevation Satellite-2 (ICEsat-2), matching, rational polynomial coefficients, satellite geometric positioning.**

I. Introduction

ADVANCED remote sensing techniques, such as multimodal cooperation, multitemporal fusion, multiview imaging, and multiscale linkage, have dramatically enhanced earth observation. These innovations have transformed how data is collected and processed for various geospatial applications. This has led to the exploration of combined adjustments utilizing multisource satellite data for enhanced photogrammetry mapping accuracy [1], [2], [3].

Received 25 May 2024; revised 2 August 2024 and 18 September 2024; accepted 8 October 2024. Date of publication 16 October 2024; date of current version 8 November 2024. This work was supported in part by the National Natural Science Foundation of China under Grant 4230142 and Grant 42171341. *(Corresponding author: Yonghua Jiang.)*

Shaodong Wei, Miaozhong Xu, and Guo Zhang are with the State Key Laboratory of Information Engineering in Surveying, Mapping, and Remote Sensing, Wuhan University, Wuhan 430079, China (e-mail: weishaodong@whu.edu.cn; mzxu6319@whu.edu.cn; guozhang@whu.edu.cn).

Yonghua Jiang is with the School of Remote Sensing and Information Engineering, Wuhan University, Wuhan 430079, China (e-mail: jiangyh@whu.edu.cn).

Bin Du and MeiLin Tan are with the Inner Mongolia Autonomous Region Surveying and Mapping Geographic Information Center, Hohhot 010050, China (e-mail: bindu@outlook.com; tanmeilin@whu.edu.cn).

Weiqi Lian is with Information Engineering University, Zhengzhou 450001, China (e-mail: lianweiqi@whu.edu.cn).

Digital Object Identifier 10.1109/JSTARS.2024.3481449

A key pursuit lies in improving the geometric positioning accuracy of optical satellites, which is typically lower than other data sources. Laser altimetry systems (LASs), such as NASA's Ice, Cloud, and Land Elevation Satellite (ICESat) [4] and the Ice, Cloud, and Land Elevation Satellite-2 (ICESat-2) [5] can obtain precise surface elevation data with accuracy better than 1m on the whole [6], [7], [8], for their high ranging accuracy. ICESat-2 also have the better horizontal accuracy (about 5 m) [9], [10]. They are significantly outperforming the positioning capabilities of optical satellites like ZY-3 (10 m in horizontal direction, 5 m in vertical direction) [11]. Thus, the higher accuracy of ICESat-2 data makes it an essential source of control points both in horizontal and vertical.

In practice, LASs data has been primarily used as vertical control points [13], [14], [15], [56], [58]. However, in areas with undulating terrain, such as mountains and hills, vertical accuracy decreases because the same horizontal shift leads to greater vertical error in these regions. To reduce vertical error, laser footprint images are aligned with optical images when reference digital orthophotos (DOM) or footprint cameras are available [16], [17], [18]. Unfortunately, many LASs, such as ICESat-1/2, lack footprint cameras, with only a few satellites, such as GF-7, possessing them. Consequently, some researchers have attempted to improve planar accuracy by incorporating SAR imagery. However, publicly available high-precision SAR data are difficult to obtain [53], [54]. In [55], the vertical accuracy of ICESat-2 control points was improved by aligning building edges with ICESat-2 data in urban areas; however, this approach is not feasible in non-urban regions. Therefore, when unknown horizontal offsets exist between LASs data and optical imagery, mainstream methods employ slope or flatness analysis to filter laser points from non-flat areas. Even if horizontal errors cause elevation inaccuracies, the effect is minimal in these regions, allowing laser points to be projected onto images to generate vertical control points for combined adjustment [19], [20], [21], [22], [23], [57].

These filter-based methods is crude, for wasting valuable information from nonflat areas. What is more, they failed to use ICESat-2's high horizontal accuracy (about 5 m) [9], [10]. Recent research has attempted to match ICESat-2 data with stereo satellite optical images before performing combined adjustments by point cloud registration methods [37], [38]. Point

© 2024 The Authors. This work is licensed under a Creative Commons Attribution-NonCommercial-NoDerivatives 4.0 License. For more information, see https://creativecommons.org/licenses/by-nc-nd/4.0/

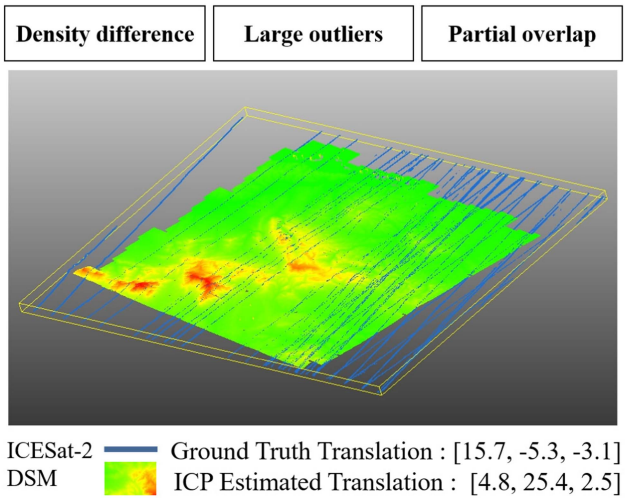

Fig. 1. ICESat-2 is directly matched with digital surface models (DSMs) generated from stereo optical satellite images, but the matching results are significantly compromised by gross errors, initial value conditions, and the quantity of point clouds.

cloud registration methods [24], [25] generally fall into three categories: optimization-based methods [26], [27], [28], [29], feature-based methods [30], [31], [32], and deeplearning-based methods [33], [34]. However, these techniques are typically designed for same-source point clouds. The ICESat-2 points clouds and point clouds form stereo satellite optical images are typical cross-source point clouds. The cross-source point clouds posed unique challenges, including large outliers, density differences, partial overlap, large rotation, and scale differences [24], [36]. When matching ICESat-2 data with stereo satellite optical images, although satellite geometric calibration provides reasonable initial positioning capabilities, minimizing issues related to large rotation and scale differences, the challenges posed by large outliers, density differences, and partial overlap are more severe, as shown in Fig. 1.

Specifically, for feature-based methods, the sparsity of ICESat-2 point clouds makes it difficult to extract suitable features. Deeplearning-based methods are data-driven but often rely on same-source point cloud datasets, with few cross-source datasets relevant to this scenario. Conversely, optimization-based methods are theoretically well-suited to this context. The latest approaches for matching ICESat-2 with stereo satellite optical image data typically use optimization-based methods [37], [38]. In [37], a method based on terrain similarity [specifically, the minimum standard deviation of the elevation difference between digital surface models (DSMs) from stereo optical satellite images and ICESat-2 data] was proposed after preprocessing ICESat-2 data. In [38], the unmodified ICP algorithm was directly applied to match ICESat-2 data with DSMs. Both methods demonstrated improved horizontal and vertical accuracy of optical satellite images in small-scale experiments with the aid of ICESat-2 data.

However, applying these methods to large-scale data still presents challenges. Optimization-based methods require accurate initial values, which can be difficult due to inherent

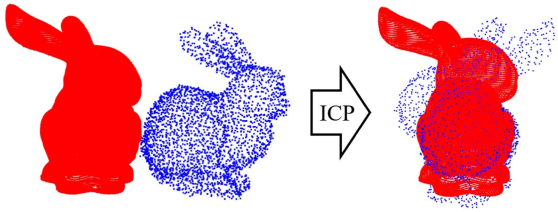

Fig. 2. Density differences alone can easily cause divergence in optimization-based point cloud registration methods.

positioning errors (ranging from a few meters to tens of meters) in large-area optical imagery. Additionally, significant discrepancies in point cloud density (with differences reaching thousands of times between ICESat-2 point clouds and DSMs) hinder convergence [28], as shown in Fig. 1. To investigate the reasons for the failure of optimization-based methods in our scenario, we conducted a simulation experiment depicted in Fig. 2. The experiment simulated two characteristics of ICESat-2 point clouds and DSMs: 1) The density of the blue point cloud for matching is reduced by a factor of 20 compared with red one to simulate the significant difference in quantity between ICESat-2 and DSM point clouds; 2. Gaussian noise with a variance of 0.0001 are added to simulate gross errors between them. The results for the ICP registration, a optimization-based method, of ICESat-2 and DSM point clouds in Fig. 2 demonstrate a substantial error which is consistent with reference [28]. In our scenario, despite cropping, the disparity in the number of points between ICESat-2 and DSMs point clouds remains thousands of times larger. And the errors from time-varying factors exceed the added Gaussian noise. This highlights the limitations of using the optimization-based method in our scenario.

Furthermore, we reviewed current cross-source point cloud registration methods [24]. The most cross-source point cloud registration methods rely on preprocessing steps to simplify cross-source registration complexity to the level of same-source registration, and then utilizing same-source point cloud registration techniques. Meanwhile, these methods are still in their infancy, as they suffer from limitations in both efficiency and accuracy, which prevents their real-world application. These methods primarily achieve practical efficiency through downsampling, which results in a significant loss of accuracy. As shown in Table II, the comparative experiments indicate that existing point cloud registration methods [26], [29], [36] exhibit significant deficiencies in accuracy and stability in our scenario.

While common point cloud registration methods are not applicable to this scenario, we found a simple yet practical method: the terrain profile elevation sequence similarity. This technique is used in extraterrestrial mapping of laser altimeter data and stereo satellite images [39]. In [39], they move laser altimeter data in the latitude and longitude directions to find the most similar profile location, achieving successful matching of LOLA with LRO wide angle camera DTMs, Mars orbiter laser altimeter with the high-resolution stereo camera, and Mercury laser altimeter with Mercury dual imaging system. Although they did not analyze why this simple method can replace point cloud registration that considers rotation, translation, and scale.

TABLE I
DETAILS OF SURVEY AREA DATA

Subject	Survey areas	Satellite Optical Images				ICESat-2			Check Data	
		Source	~GSD/m	Number	Time	Source	Num/Orbit	Time	Type	Number
Matching	Baotou	JL-1	1	2	2022	ATL03/08	62	2019–2023	Datum DOM/DEM	20
	Chifeng	GF-7	0.65/0.8	2	2022	ATL03/08	50	2018–2023	Datum DOM/DEM	19
	Nanjing	ZY-3	2.5	2	2015	ATL03/08	47	2018–2022	GPS	11
	Songshan	ZY-3	2.5	2	2019	ATL03/08	66	2018–2023	Datum DOM/DEM	9
	Ganzhou	ZY-3	2.5	2	2013	ATL03/08	23	2019–2022	GPS	9
Large-scale BA	Hubei	TH-1	4.6	297	2014	ATL03/08	137	2018–2023	GPS	128
	Jiangxi	ZY-3	2.5	255	2018	ATL03/08	122	2018–2023	GPS	131

TABLE II
COMPARISON OF MATCHING METHODS

			Baotou	Chifeng	Nanjing	Songshan	Ganzhou
Ground Truth	Lat/m		18.1	2.2	1.7	8.3	−4.3
	Lon/m		17.9	−7.5	8.2	3.5	−5.3
ICP [26]	Matched	Lat/m	−16.3	−298	0.1	−39.6	−93.7
		Lon/m	−10	7.4	−0.3	29.7	−25.7
	Error	Lat/m	−34.4	−300.2	1.8	−47.9	−89.4
		Lon/m	−27.9	14.9	7.9	26.2	−20.4
Robust-ICP [29]	Matched	Lat/m	−1.2	172.9	−1.6	40.4	−144.5
		Lon/m	10.2	−53.4	5.7	17.7	−82.7
	Error	Lat/m	19.3	−170.7	3.3	−32.1	140.2
		Lon/m	7.7	45.9	2.5	−14.2	77.4
GCTR [36]	Matched	Lat/m	20.7	*	3	*	*
		Lon/m	16.2	*	4.7	*	*
	Error	Lat/m	−2.6	*	−1.3	*	*
		Lon/m	1.7	*	3.2	*	*
Ours	Matched	Lat/m	19.7	4.3	0.2	6.9	−3.6
		Lon/m	18.3	−9.2	6.6	5.5	−8.2
	Error	Lat/m	1.6	2.1	−1.5	−2.3	0.7
		Lon/m	0.4	−1.7	−1.6	1.9	−2.9

* represents divergence result

We analyzed the registration of spaceborne lidar altimetry point clouds and DSMs point clouds generated from stereo satellite optical images, with the following observations: Satellite imagery has good initial accuracy due to geometric calibration, minimizing the need for rotational alignment and focusing primarily on translation, with almost no scale issues. Thus, in this context, point cloud registration simplifies from estimating rotation, translation, and scale to solving only for translation. Furthermore, when using the Z-direction elevation profile as a feature, the search space for final matching is reduced to horizontal displacement in the latitude and longitude directions. At this stage, point cloud registration has shifted from seeking a local optimum in the solution space of rotation, translation, and scale to employing a global search method that traverses the known range to find the global optimum. The convergence and robustness of this global traversal approach are superior to optimization methods.

However, a key challenge remains: extraterrestrial mapping, such as on Mars and the Moon, typically involves bare surfaces with minimal vegetation, seasonal changes, or significant human activity. In contrast, ICESat-2 data used for large-scale Earth mapping are often multitemporal. As shown in Fig. 3, the complex and temporally varying nature of Earth's surface topography introduces numerous outliers in terrain profile elevation sequences, caused by changes in vegetation, water bodies, snow cover, and surface structures [40]. To address this, we removed outliers at multiple stages during the matching. Despite these removals, the registration performance of each ICESat-2 orbit varies due to differences in terrain features, temporal changes, or gross errors in the imagery. These

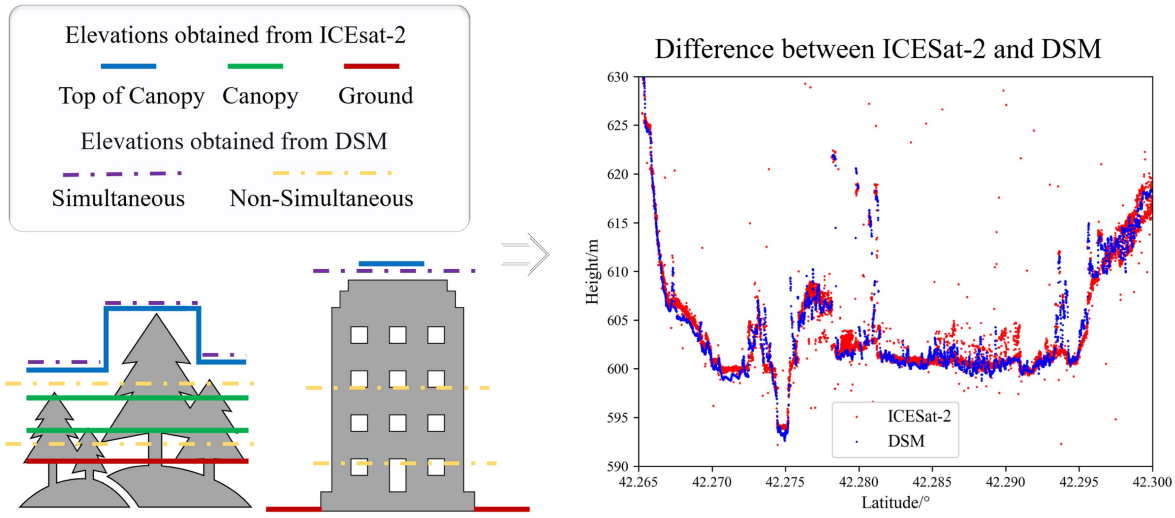

Fig. 3. ICESat-2 and optical digital surface model (DSM) provide elevation information with differences. Laser altimetry from ICESat-2 penetrates vegetation, while optical imagery used for DSM generation does not. This leads to discrepancies in the captured elevation. Furthermore, temporal discrepancies between data acquisitions due to vegetation growth, human activities, and instrument limitations can introduce uncertainties in pinpointing the exact source of the elevation measurement (surface, canopy, or top of canopy).

TABLE III
COMPARATIVE EXPERIMENT OF MATCHING METHODS FOR DIFFERENT PROCESSES

Method		Baotou	Chifeng	Nanjing	Songshan	Ganzhou
Without DEM assisted pre-correction	Lat/m	2.42	1.79	−1.53	−3.28	−1.79
	Lon/m	−1.13	−3.23	−1.71	2.57	−3.78
With height difference similarity	Lat/m	2.37	−1.94	−1.72	−1.97	−0.98
	Lon/m	0.75	4.45	−2.87	5.96	7.72
Without robust Gaussian fitting extraction	Lat/m	−3.15	2.89	3.31	−3.38	−0.74
	Lon/m	−0.92	−3.58	4.8	1.51	−3.71
With Z-score (threshold:3)	Lat/m	1.72	2.93	−1.49	−2.74	−1.88
	Lon/m	0.44	−1.61	−1.64	3.14	−4.91
DEM assisted pre-correction + Z-score (threshold:2) + robust Gaussian fitting extraction	Lat/m	1.57	2.05	−1.48	−2.33	0.69
	Lon/m	0.39	−1.65	−1.56	1.96	−2.91

variations result in inconsistent control performance from the matched ICESat-2 data. Existing adjustment methods do not account for such prior information. In response, we incorporated these uncertainties into a weight for combined adjustments, significantly improving the accuracy of the adjustment process.

The contributions of this article are as follows.

Contribution 1: We improved the registration method for ICESat-2 and stereo satellite optical imagery to address the complex conditions of large-area data. This includes eliminating point cloud rotational errors through digital elevation model(DEM) adjustments, removing significant outliers using the Z-score method, and designing a robust Gaussian fitting method to ensure sub-pixel accuracy and provide more precise registration. In Section III-B, we conducted ablation experiments to demonstrate the effectiveness of each component, with results presented in Table III.

Contribution 2: To address the issue of varying matching performance caused by diverse terrain and temporal differences across large areas, we introduced a novel combined adjustment weight strategy that accounts for matching uncertainties. We use the two-dimensional (2-D) Gaussian sigma parameters as indicators of matching confidence, transforming them into weights for the combined adjustment. In Section III-C, we compare the results, showing improvements in planar accuracy from 4.72 to 4.24 m and elevation accuracy from 1.86 to 1.67 m in the Hubei test area, as well as improvements in planar accuracy from 3.88 to 3.46 m and elevation accuracy from 1.69 to 1.53 m in the Jiangxi test area.

Contribution 3: We achieved successful registration and combined adjustment of ICESat-2 and optical imagery over large areas with significant temporal differences (4–9 years in Hubei and 1–5 years in Jiangxi). Existing methods typically apply to small areas with only one or a few scenes, often fewer than six. These methods also work best when temporal variation between datasets is minimal, usually between 0 and 3 years. Our experiments demonstrate that even in large provincial regions, with a temporal gap of up to 9 years between laser and optical

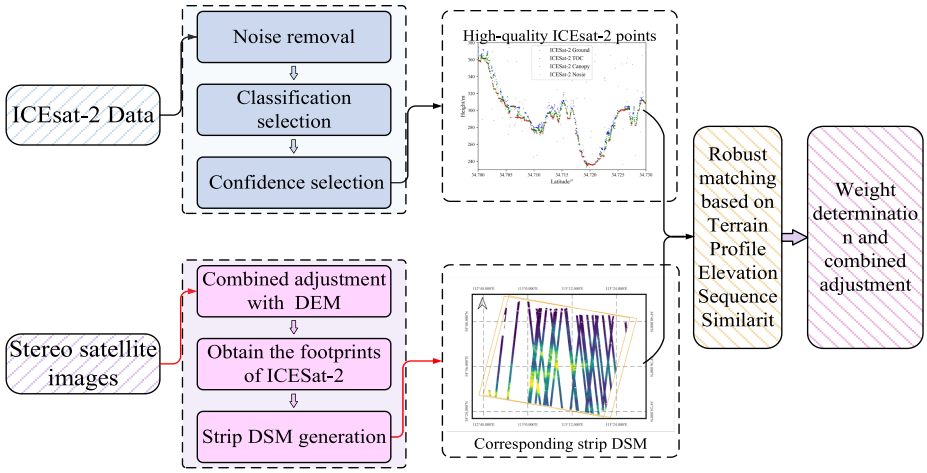

Fig. 4. Large-area ICESat-2 data and stereo satellite images combined adjustment pipeline.

imagery, high accuracy can still be achieved. This provides a valuable reference for future work.

II. Methodology

Matching ICESat-2 data with DSMs using the ICP method faces limitations, especially due to poor initial values and large discrepancies in point numbers. To address this, we adopted a terrain profile similarity-based method (see Section II-A). However, this approach tends to have low matching accuracy due to its susceptibility to gross errors caused by time-varying factors. To improve this, we implemented a more robust similarity measure (see Section II-A-2) and an enhanced matching point extraction algorithm (see Section II-A-3). And then, we discovered that heatmaps generated from the matching process reflect variations in matching accuracy, providing valuable information for more precise adjustments (Section II-A). The entire process is detailed in Fig. 4.

A. Matching Between ICESat-2 Data and Stereo Satellite Images

1) Preprocessing of ICESAT-2 Data: ICESat-2 was launched as a NASA mission in 2018 to measure Earth's ice, land, and vegetation elevations using the advanced topographic laser altimeter system (ATLAS). ATLAS emits laser pulses to capture precise elevation data, which is crucial for understanding climate change impacts.

ICESat-2 produces two main data products: ATL03 and ATL08. ATL03 offers high-resolution, geolocated photon data at a 17-m resolution, whereas ATL08 provides a coarser 100-m resolution, classifying surface types. The data products generated by ICESat-2 support studies in cryosphere dynamics, land topography, forest structure, hydrology, and climate change. ICESat-2's detailed measurements enhance our comprehension of Earth's dynamic systems, informing climate and environmental policies [5].

Despite the high density of ATL03 data, inherent noise can hinder matching performance. Therefore, we use PhoReal software [40] for classification and denoising, utilizing ATL08 mapping information, as shown in Fig. 5. We retain points classified as surface, vegetation, or canopy, provided their confidence level exceeds 2 (medium to high quality).

2) Preliminary Geometric Correction and Stripe DSM Generation: Based on the methodology in [3], we integrate Copernicus digital elevation models 30 m (Cop-30) with optical satellite imagery for combined adjustments, which offers the highest accuracy among publicly available 30-m DEMs [42]. Cop-30 is a global elevation dataset produced by the European Space Agency as part of the Copernicus program. Derived from TanDEM-X satellite data, it provides detailed 30-m spatial resolution data of Earth's surface, supporting applications in environmental monitoring, flood modeling, terrain analysis, and urban planning. The dataset's high accuracy and open-access policy make it a valuable tool for scientific research, disaster response, and sustainable development efforts worldwide.

Using the Copernicus DEM 30 m in conjunction with stereo satellite optical imagery for combined adjustment represents a technique designed to eliminate geometric positioning errors of satellite camera model roughly. By aligning the DEM with the stereo imagery, discrepancies in elevation and positioning caused by sensor inaccuracies or terrain distortions are corrected. Specifically, by reading the height values from the DEM, the object-space coordinates of tie points, identified through image matching, are used to generate elevation control points. The combined adjustment process then employed these height control points along with tie points to refine the alignment between the datasets, leading to improved accuracy. This method effectively eliminates vertical, pitch, and roll offsets between the point cloud and its true position, and due to the characteristics of satellite imaging, the yaw angle is typically negligible.

Next, we generate DSMs and point clouds from the stereo imagery using the S2P [43], a satellite 3-D reconstruction library. To optimize computational efficiency for large-scale data processing, we create strip DSMs localized near ICESat-2 data

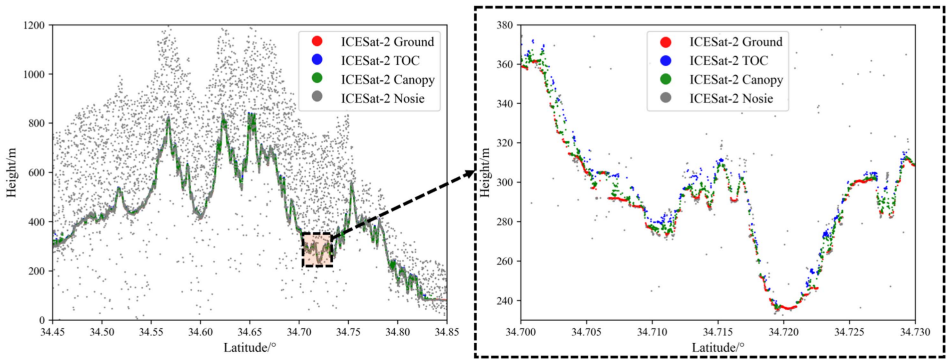

Fig. 5. ICESat-2 data classification results show that the original ATL03 product is divided into four types. In this study, we retained only the ground, canopy, and top of canopy classifications, while gray noise points were removed.

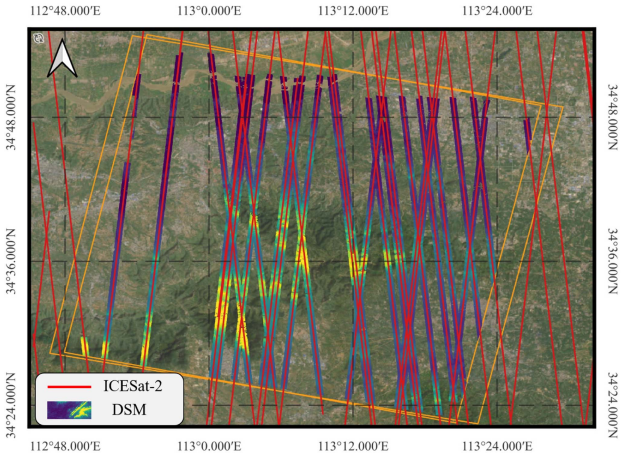

Fig. 6. Local stripe DSM generated from satellite images for corresponding ICESat-2 data.

tracks as visualized in Fig. 6. This strategy leverages two key aspects: 1) ICESat-2 data is distributed in six roughly straight lines, and 2) there is a relatively small initial geographic offset (typically less than 100 m) between ICESat-2 and optical satellite image. While maintaining accuracy, this approach minimizes resource consumption, as demonstrated by the time performance analysis in Section III-D.

3) Robust Matching Base on Terrain Profile Elevation Sequence Similarity: With the preprocessed ICESat-2 points and corresponding DSMs, the matching task becomes on identifying the most similar locations in two horizontal directions. The matching, based on terrain profile elevation sequence similarity, involves two steps.

1) *Horizontal translation and similarity heatmap generation (See Fig. 7):* We iteratively translate ICESat-2 points horizontally on the DSM, generating elevation vectors for both datasets. The corresponding elevation value on the DSM for each translated ICESat-2 point is obtained using bilinear interpolation. A similarity measure is then calculated at each position, resulting in a heatmap.
2) *Matching position extraction (See Fig. 9):* The heatmap reflects the terrain profile elevation sequence similarity between the data sets at various horizontal offsets. The ideal matching result corresponds to the peak locations in the heatmap. In order to improve matching accuracy, subpixel matching accuracy is often required, but refining the search step size will result in a time consumption of square times, so we perform center point fitting. Meanwhile, outliers can introduce inconsistent. We also need to consider this.

a) Robust similarity: After obtaining the series of ICESat-2 point elevations on the DSM by moving in horizontal, we get two sequence of elevation vectors $\mathcal{H}^{\text{ICES } S_{at}} = \{h_n^{\text{ICESat}} \mid n = 1, 2 \ldots N\}$ and $\mathcal{H}^{\text{DSM}}{}_i = \{h_n^{\text{DSM}} \mid n = 1, 2 \ldots N\}$ where $h_n^{\text{DSM}}(\Delta\text{lon}, \Delta\text{lat}) = \tau(\text{lon}_n + \Delta \text{ lon }_n, \text{lat}_n + \Delta \text{ lat }) \in \mathbb{R}$ the corresponding elevation value on the DSM when moving Δlon, Δlat in horizontal.τ is a bilinear interpolation. n and N are the serial number and total number of ICEsat-2 points.

To reduce outliers commonly present in time-varying remote sensing data, we employ the Z-score method for outlier detection and removal. Points with Z-scores exceeding a predefined threshold (set to 2 in this work) are identified and excluded. Subsequently, Pearson correlation [45], a robust metric less susceptible to outliers compared to elevation difference methods, is used to measure similarity. The formula for the Pearson correlation coefficient r is as follows:

$$r = \frac{\sum \left(\mathcal{H}^{\text{ICESat}}{}_i - \overline{\mathcal{H}^{\text{ICESat}}}\right)\left(\mathcal{H}^{\text{DSM}}{}_i - \overline{\mathcal{H}^{\text{DSM}}}\right)}{\sqrt{\sum \left(\mathcal{H}^{\text{ICESat}}{}_i - \overline{\mathcal{H}^{\text{ICESat}}}\right)^2 \sum \left(\mathcal{H}^{\text{DSM}}{}_i - \overline{\mathcal{H}^{\text{DSM}}}\right)^2}} \tag{1}$$

where $\overline{\mathcal{H}^{\text{ICESat}}}$ and $\overline{\mathcal{H}^{\text{DSM}}}$ are the means.

After calculating the similarity of each moving position, a heatmap depicting the terrain profile elevation sequence similarity will be generated. Fig. 8 demonstrates that by translating the ICESat-2 data in the longitude and calculating the similarity with DSM, the extremum similarity of the Pearson Correlation measure is closer to the true value compared to the elevation difference. Furthermore, the sharper peaks of the Pearson Correlation measure indicate that the similarity difference between correct and incorrect positions is more pronounced.

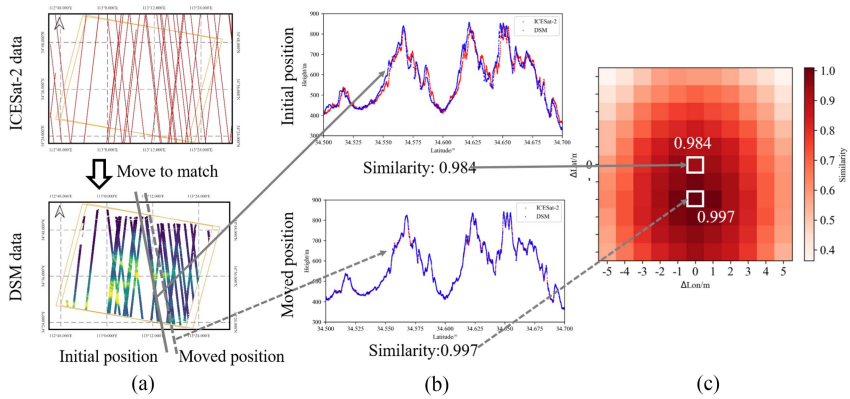

Fig. 7. Horizontal translation and similarity heatmap generation for matching. The color bar values represent different contour similarities, ranging from 0 to 1. The redder areas indicate a higher similarity score, meaning that the profiles between the laser data and DSM are more closely matched in these regions. (a) Input Data and matching. (b) Local visualization of terrain profile elevation sequence similarity. (c) Similarity heatmap.

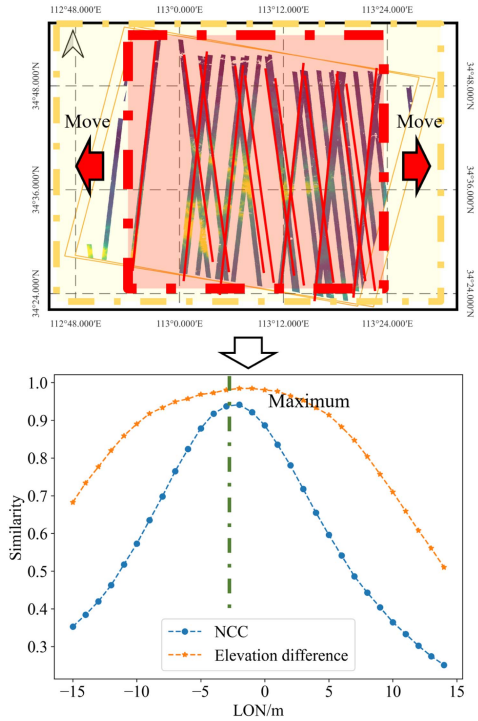

Fig. 8. Comparison of matching similarity results between elevation difference and Pearson correlation when moving longitude direction.

b) Robust matching position extraction: Once the similarity heatmap is obtained, accurate matching location extraction is crucial. We compare commonly used methods, including the maximum value method, grayscale centroid method [47], and 2-D Gaussian fitting with orientation [48].

Fig. 9 illustrates the comparison of these methods. In actual heatmap, it reveals that 2-D Gaussian fitting with a robust kernel outperforms other methods. The maximum value methods in A and B were both affected by incorrect extreme values and failed to utilize the trend of the heatmap. Additionally, when the heatmap in B is incomplete, the grayscale centroid method also extracts an incorrect center. In contrast, our Gaussian center fitting method with a robust loss function effectively addresses both incomplete heatmaps and outliers, leading to more accurate spot center extraction.

The general form of a 2-D rotated Gaussian function is given by the following:

$$z(x,y) = A\exp\left(-\left(\begin{array}{c} a(x-x_0)^2+ \\ 2b(x-x_0)(y-y_0)+c(y-y_0)^2 \end{array}\right)\right) \tag{2}$$

where

A is the amplitude.

x_0, y_0 are the coordinates of the center of the Gaussian.

a, b, c are coefficients that depend on the standard deviations σ_x, σ_y along the x and y axes and the rotation angle θ, calculated as follows:

$$\begin{aligned} a &= \frac{\cos^2\theta}{2\sigma_x^2} + \frac{\sin^2\theta}{2\sigma_y^2} \\ b &= -\frac{\sin 2\theta}{4\sigma_x^2} + \frac{\sin 2\theta}{4\sigma_y^2} \\ c &= \frac{\sin^2\theta}{2\sigma_x^2} + \frac{\cos^2\theta}{2\sigma_y^2}. \end{aligned} \tag{3}$$

We use least squares estimation for fitting and enhance its robustness to outliers by incorporating additional robust kernel, enabling the retrieval of accurate central coordinates.

B. Combined Bundle Adjustment

We account for the inherent errors in ICESat-2 control points by treating them as weighted observations with object space constraints during the bundle adjustment. This least-squares approach minimizes reprojection error as well as deviations in ground coordinates. To improve robustness and eliminate the influence of dimensional differences, we perform the adjustment in a normalized coordinate system derived from the rational polynomial coefficients associated with each image [49][50]. The optimization loss function is defined as follows:

$$V = AT + BX - L, P \tag{4}$$

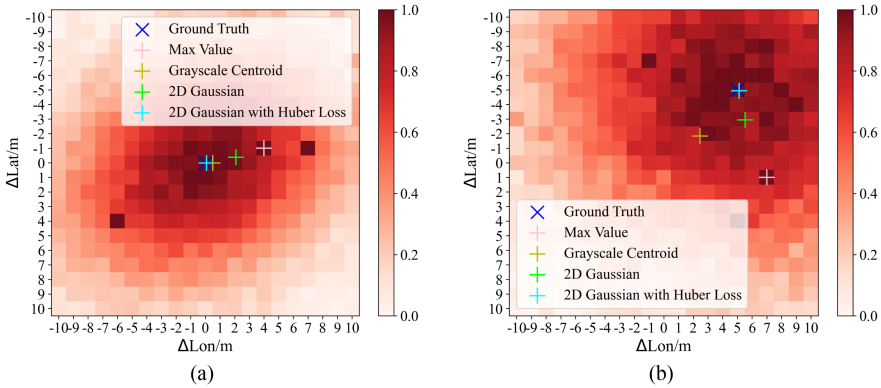

Fig. 9. Comparison of matching position extraction methods.

$T = [\Delta a_0 \Delta a_1 \Delta a_2 \Delta b_0 \Delta b_1 \Delta b_2]^T$ is the correction vector of the affine transformation parameters,

$X = [\Delta\phi \Delta\lambda \Delta h]^T$ is the correction vector of the ground point coordinates, ϕ, λ, h is the normalized ground coordinate parameter of longitude, latitude, and elevation.

The observation V is the vector of residual errors from all tie points, A is the coefficient matrices for affine parameter correction, and B is the coefficient matrices for ground coordinate correction. They contain the partial derivatives of parameters.

Where

$$A_1 = \begin{bmatrix} \frac{\partial s}{\partial a_0} & \frac{\partial s}{\partial a_1} & \frac{\partial s}{\partial a_2} & 0 & 0 & 0 \\ 0 & 0 & 0 & \frac{\partial l}{\partial b_0} & \frac{\partial l}{\partial b_1} & \frac{\partial l}{\partial b_2} \end{bmatrix} \tag{5}$$

$$B_1 = \begin{bmatrix} \frac{\partial s}{\partial \phi} & \frac{\partial s}{\partial \lambda} & \frac{\partial s}{\partial h} \\ \frac{\partial l}{\partial \phi} & \frac{\partial l}{\partial \lambda} & \frac{\partial l}{\partial h} \end{bmatrix}. \tag{6}$$

P is the weight matrix. In this article, the weight matrix assigned to the optical tie points is uniform, while the weights for the control points are determined by the matching error σ_{Matching}.

The 2-D Gaussian sigma (standard deviation) and orientation obtained during subpixel matching (see Section II-A-3) serve as an indicator of matching confidence. Spots with higher concentration and smoother distributions in the heatmap represent more reliable matches. We use this anisotropic confidence information to guide the bundle adjustment.

To incorporate this uncertainty into a combined adjustment framework, we derive a weight matrix P based on the inverse of the covariance matrix Σ, which encapsulates the uncertainty information.

The covariance matrix for the rotated Gaussian distribution is given by the following:

$$\boldsymbol{\Sigma} = \begin{bmatrix} \sigma_x^2 \cos^2\theta + \sigma_y^2 \sin^2\theta & \left(\sigma_x^2 - \sigma_y^2\right) \cos\theta \sin\theta \\ \left(\sigma_x^2 - \sigma_y^2\right) \cos\theta \sin\theta & \sigma_x^2 \sin^2\theta + \sigma_y^2 \cos^2\theta \end{bmatrix}. \tag{7}$$

The inverse of the covariance matrix, which forms the basis of the weight matrix, is as follows:

$$\boldsymbol{\Sigma}^{-1} = \frac{1}{\sigma_x^2 \sigma_y^2} \begin{bmatrix} \sigma_y^2 \cos^2\theta + \sigma_x^2 \sin^2\theta & -\left(\sigma_x^2 - \sigma_y^2\right) \cos\theta \sin\theta \\ -\left(\sigma_x^2 - \sigma_y^2\right) \cos\theta \sin\theta & \sigma_x^2 \cos^2\theta + \sigma_y^2 \sin^2\theta \end{bmatrix}. \tag{8}$$

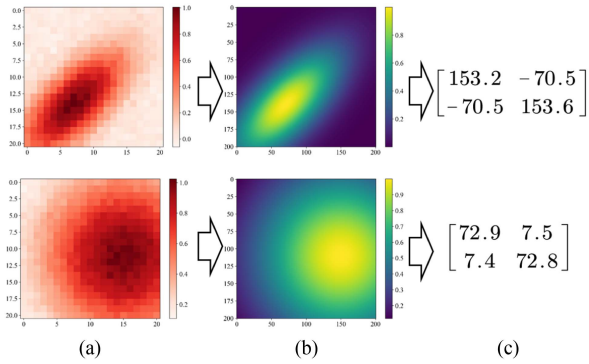

Fig. 10. Fit 2-D Gaussian and corresponding weights from the matching heatmap.

The weight matrix P is thus defined as follows:

$$P = \Sigma^{-1}. \tag{9}$$

Specifically, we move the 2-D Gaussian center to (0,0), followed by obtaining covariance matrix calculation and weight matrix by inversion (see Fig. 10). This weight matrix is incorporated into a generalized least squares problem [46] formulated with Huber robust loss function [51] to account for potential outliers. Solving this system yields the final geometric correction results.

III. Experiments

A. Data Description

We employed stereo optical imagery from four satellites: Jinlin-1, GF-7, ZY-3, and TH-1. The ATL03 and ATL08 product from ICESat-2 was used.

1) Matching Experiment Sites: Five test regions across China were chosen: Baotou, Chifeng, Nanjing, Songshan, and Ganzhou. Baotou, Chifeng, and Songshan encompass urban, plain, and mountainous areas, while Nanjing and Ganzhou represent typical urban and mountainous landscapes, respectively. This selection allows us to evaluate the algorithm's performance across varied terrains. The survey areas include 1:2000-scale DOM, DEM, or GPS reference points for verification.

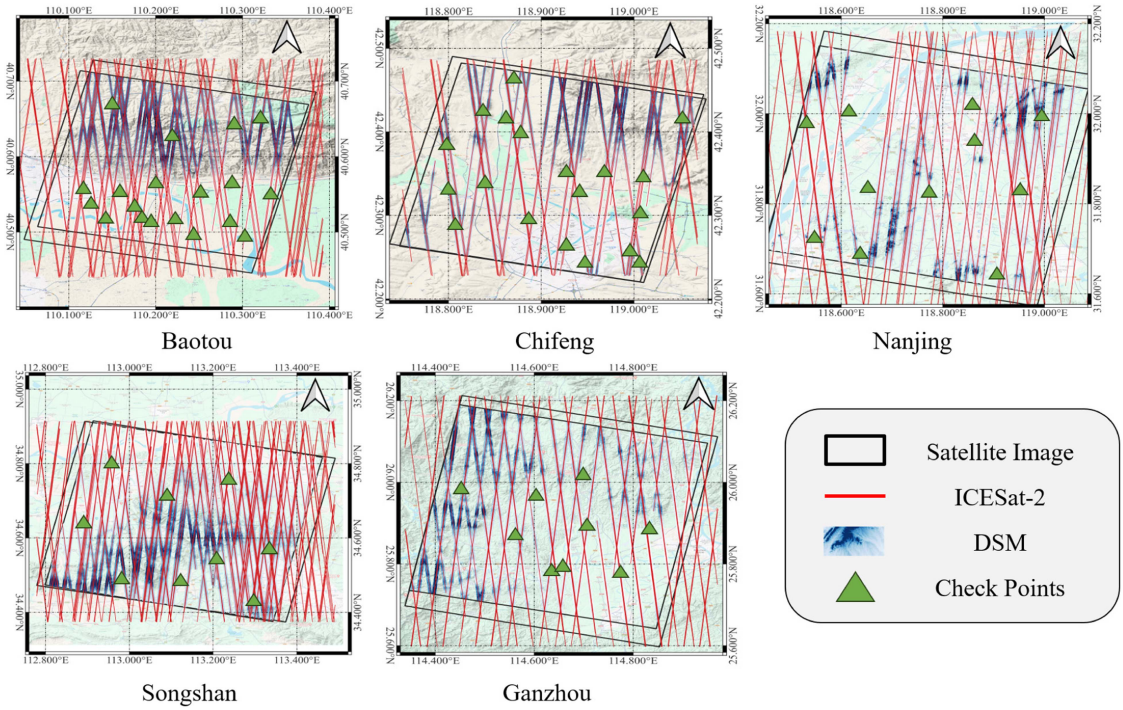

Fig. 11. Details of matching experimental, The black quadrilateral represents the optical satellite image, the red points represent ICESat-2 data, the blue raster image is DSM, and the green triangle represent the check points.

2) Combined Adjustment Experiment Sites: Two large regions were selected for combined bundle adjustment: Hubei Province (108.3661–116.1327 E, 29.0994–33.3364 N, area: 187 500 km²) and Jiangxi Province (113.5619–118.4569 E, 24.484–30.10 N, area: 167 000 km²). These areas, encompassing mountains, hills, and plains, provided a comprehensive testing ground and included GPS control points with sub-centimeter accuracy for verification.

The diverse landforms in Hubei and Jiangxi, ranging from mountainous regions to lowland plains, provide a comprehensive foundation for assessing the algorithm's adaptability across various terrain conditions. These regions also encompass a broad spectrum of land cover types, including forests, agricultural fields, urban areas, and water bodies. This allows for a thorough evaluation of the algorithm's potential for wider geographical application. The dataset covers a temporal range of 1–9 years, capturing seasonal variations, vegetation dynamics, and human activity across the regions. This temporal diversity tests the algorithm's robustness by assessing its ability to handle significant temporal changes.

We employed the scale-invariant feature transform [52] algorithm for automated tie point matching between optical images. Pixel locations on stereo satellite images of ICESat-2 points were obtained through template matching. Details are provided in Figs. 11, 12, and Table I.

B. Matching Experiment and Evaluation

The matching performance determines the accuracy of the combined adjustment, and higher planar accuracy also means higher vertical accuracy. Direct comparison of the matching accuracy of ICESat-2 data for each track is challenging due to the lack of sufficient high-precision DSM for error evaluation. But our goal is to generate control points to improve the accuracy of optical images, so we evaluate the control ability of a set of stereo image pairs after matching with ICESat-2 through checkpoint evaluation. The results are as Table II.

Compared with the existing methods, our method has the characteristics of simplicity, robustness, and high accuracy. This demonstrated that ICESat-2 data and optical images can be more accurately aligned, leading to improved vertical accuracy.

The ICP [26] method is highly sensitive to initial values and suffers from excessive degrees of freedom due to the large discrepancies between datasets. It also requires manual parameter adjustments, making it difficult to define convergence thresholds. These issues lead to potential stagnation in some locations, such as Nanjing, or divergence in other cities.

The Robust-ICP [29] method demonstrated improved accuracy compared to the original ICP method in specific regions. Nevertheless, challenges such as large outliers, density differences, and partial overlap remain prevalent in optimization-based point cloud matching, resulting in significant errors that persist despite these improvements.

The GCTR [36] method, while designed for cross-source point cloud matching, encounters significant errors and pronounced density differences between ICESat-2 and DSM point clouds in this study. This resulted in divergence at locations such as Chifeng, Songshan, and Ganzhou. Although successful matches were achieved in Baotou and Nanjing, the downsampling feature inherent in this method led to lower accuracy compared to our proposed approach.

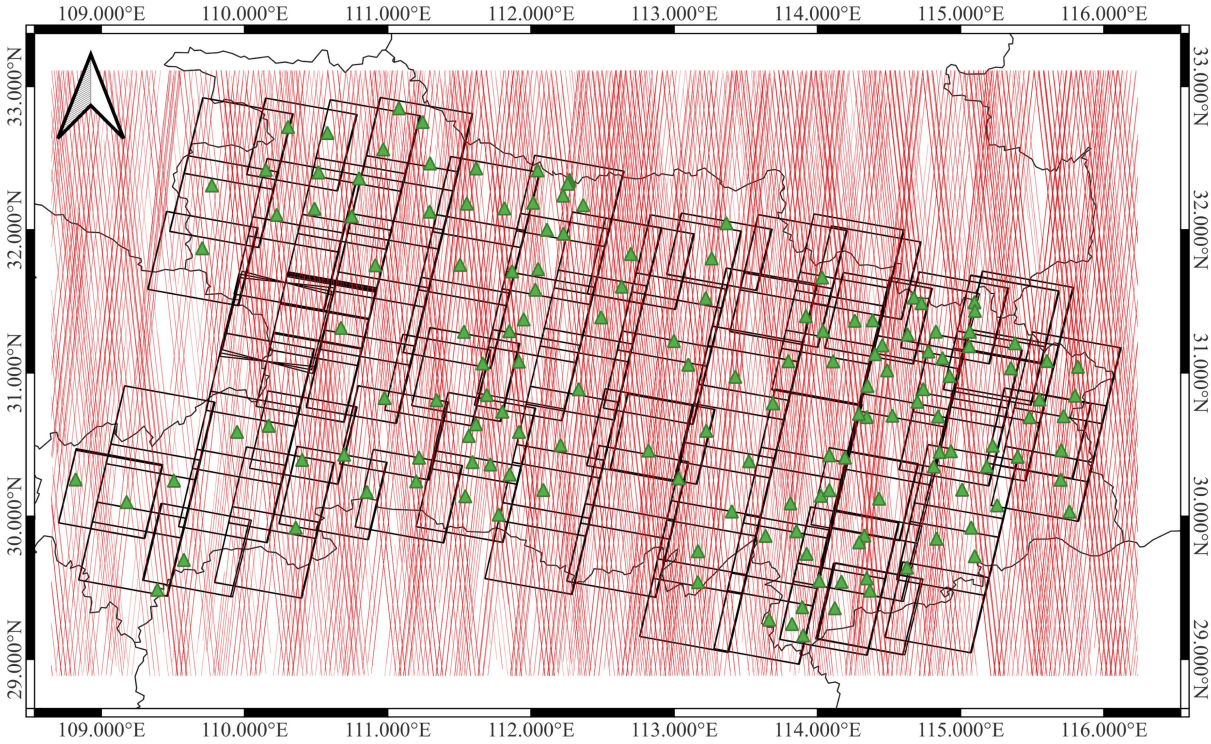

(a)

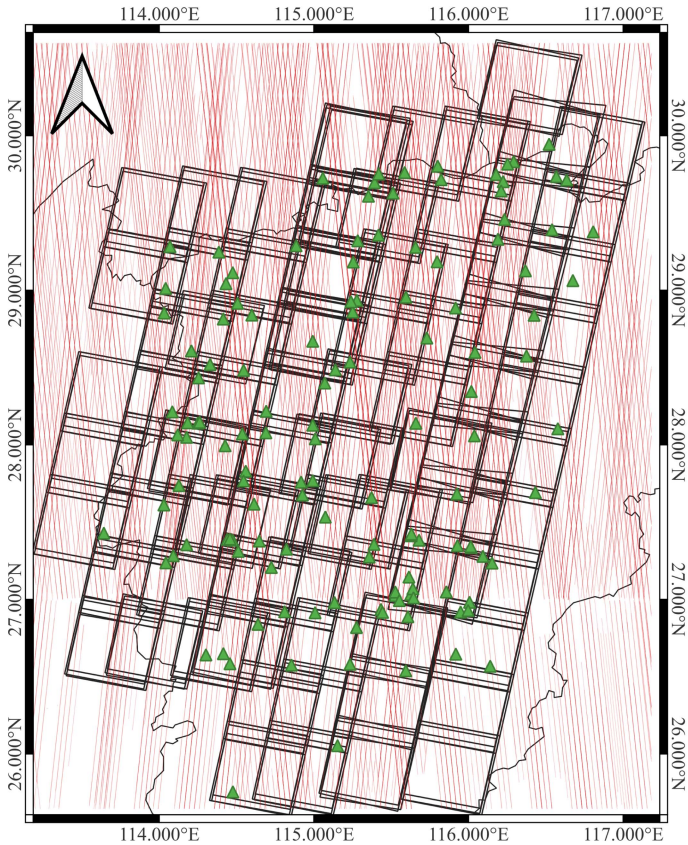

(b)

Fig. 12. Details for bunlding adjustment (BA) experiment. The black quadrangle represents the optical satellite image, the red points represent ICESat-2 ATL03 data, and the green triangle represent the check points. (a) Hubei survey area. (b) Jiangxi survey area.

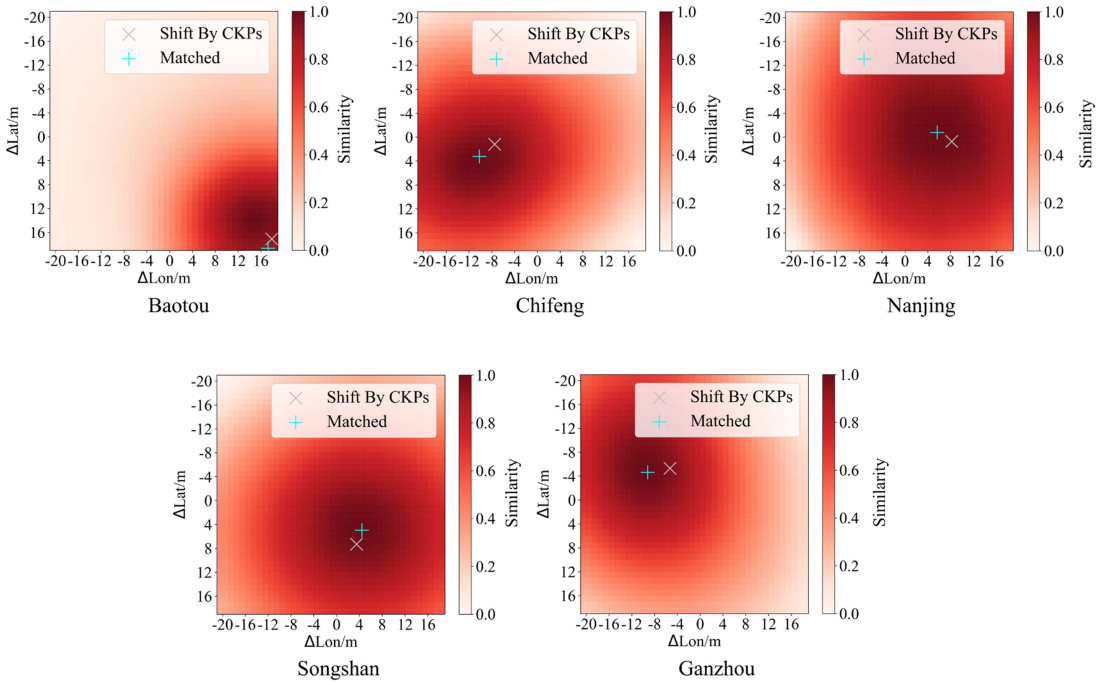

Fig. 13. Heatmaps and extraction results for the study areas. The color bar values represent similarity scores, ranging from 0 to 1. Redder areas indicate higher similarity scores, signifying a closer match between the profiles of the ICESat-2 data and the DSM at these locations.

Our proposed method, as visualized in Fig. 13, demonstrated consistent performance across diverse terrains (urban, mountainous, hilly, or combinations), various resolutions (0.7–3 m), and significant time intervals (2–7 years). Notably, it achieved planar accuracy better than 5 m using a single stereo image pair and ICESat-2 data. Moreover, our matching accuracy is theoretically higher as these results include horizontal errors inherent to ICESat-2 data.

Furthermore, we conducted ablation experiments on our improvements to demonstrate their effectiveness, with results shown in Table III.

Without DEM-assisted pre-correction, uncontrolled precision in some stereo satellite optical images resulted in varying degrees of rotational errors between ICESat-2 laser point clouds and DSM point clouds, leading to reduced registration accuracy. This demonstrated the necessity of DEM-assisted precorrection.

When the minimum elevation difference was used instead of the NCC correlation coefficient in this study, the instability of the similarity measure lead to a decrease in accuracy across all test areas. The decline were most pronounced in Songshan and Ganzhou, where seasonal vegetation changes occur.

Without using our robust Gaussian fitting method and employing existing maximum extraction methods, the matching results became integers, and the heatmap maximum skewed, causing decreased accuracy.

Finally, we tested the threshold for the Z-score method. The conventional empirical value is 3, but in this study, we found that a large amount of outlier significantly will impact matching accuracy. Therefore, we recommend a threshold of 2, which achieved better results, especially in vegetation-rich areas like Songshan and Ganzhou.

In summary, the improvements in our matching method have been proven to yield positive results, demonstrating the rationality and effectiveness of the enhancements presented in this article.

C. Combined Adjustment Experiments and Evaluation

To assess the effectiveness of our combined bundle adjustment approach, we compared its performance with that of several alternative methods in the large survey areas of Hubei and Jiangxi. We did not choose optimization-based matching approaches, because the matching produced too many divergences, rendering the results incomparable. Tables IV and V summarize the results. MIN and MAX represent the minimum and maximum absolute deviations, respectively. RMSE stands for root mean square error. We analyzed the results.

1) *Forward Intersection:* This method directly computes object space coordinates without bundle adjustment, offering no improvement due to the lack of external references for systematic errors.
2) *Free-Network Adjustment:* This approach focuses on the internal image consistency and yields limited improvement (e.g., Hubei: planimetric accuracy from 11.3 to 9.87 m, vertical accuracy from 8.2 to 6.4 m; Jiangxi: planimetric accuracy from 18.77 to 11.01 m, vertical accuracy from 14.99 to 11.52 m). These results highlight the necessity of external data for enhancing geometric positioning accuracy.
3) *COP-30 DEM Reference:* While COP-30 DEM usage improved vertical accuracy and eliminating almost all attitude errors. Its limitations included: Low resolution

TABLE IV
COMBINED ADJUSTMENT RESULT IN HUBEI

Scheme	Horizontal Accuracy (m)			Vertical Accuracy (m)		
	Min	Max	RMSE	Min	Max	RMSE
Forward intersection	0.08	30.09	11.30	0.05	23.64	8.20
Free-Network	0.07	28.97	9.87	0.00	28.29	6.40
With COP-30	0.08	30.18	10.07	0.13	10.29	2.98
Terrain Filtering	0.07	31.97	11.60	0.01	8.23	2.44
Ours without weight strategy	0.01	11.42	4.72	0.02	3.41	1.86
Ours	0.02	11.15	4.24	0.01	3.22	1.67

TABLE V
COMBINED ADJUSTMENT RESULT IN JIANGXI

Scheme	Horizontal Accuracy (m)			Vertical Accuracy (m)		
	Min	Max	RMSE	Min	Max	RMSE
Forward intersection	0.06	41.83	18.77	0.05	50.03	14.99
Free-Network	0.10	39.43	11.01	0.06	41.45	11.52
With COP-30	0.07	33.79	12.45	0.01	10.77	3.16
Terrain Filtering	0.08	31.11	12.47	0.30	12.31	2.79
Ours without weight strategy	0.01	10.65	3.88	0.03	2.74	1.69
Ours	0.01	10.86	3.46	0.04	2.65	1.53

TABLE VI
TIME CONSUMPTION AND EFFICIENCY IMPROVEMENT OF DSM GENERATION ACROSS DIFFERENT REGIONS

	Baotou	Chifeng	Songshan	Hubei	Jiangxi
Tie Point Matching (min)	4.2	5.8	3.3	173.5	265.8
DEM-Aided Bundle Adjustment (s)	2.3	3.5	1.9	20.7	16.6
ICESat-2 Preprocessing (min)	7.2	4.9	6.1	30.9	45.2
Local DSM Generation (min)	9.8	7.5	8.4	571.7	679.4
Matching between DSM and ICESat-2 (min)	2.9	1.4	2.5	127.7	168.4
Bundle Adjustment (s)	3.1	4.4	3.8	44.3	37.2
Total	26.5	23.2	22.3	925.2	1176.0
Full DSM Generation (min)	43.8	79.2	69.4	4932.6	7424.3
DSM generation time improvement ratio	77.6%	90.5%	87.9%	88.4%	90.8%

(30 m) leading to reduced accuracy; Time discrepancy between DEM (2016) and optical imagery, causing temporal errors; Inconsistency due to differing imaging bands (COP-30 penetrating ground objects, optical imagery capturing them).

4) *Terrain-Filtered ICESat-2 Projection [13], [13], [14], [15], [16], [17], [18], [19], [20], [21]:* This common method removes ICESat-2 points in uneven terrain to accommodate planimetric errors in optical images. However, the results suggest there are two limitations in this method: Inability to register the horizontal, thus offering no improvement in planimetric accuracy; Significant removal of laser points, hindering data utilization, especially in mountainous areas.
5) *Our Proposed Method:* Our approach achieved superior performance, enhancing both horizontal and vertical accuracy to 5 and 2 m, respectively (Hubei: 4.24 m horizontal, 1.67 m vertical; Jiangxi: 3.46 m horizontal, 1.53 m vertical). The matching accuracy of images is basically fixed, and low resolution will reduce the intersection accuracy of the object space. Thus, Jiangxi exhibited slightly better accuracy due to higher ground resolution of the ZY3 images compared to TH1 images used in Hubei. Additionally, incorporating a weight strategy based on matching confidence further improved geographic positioning accuracy, proving effective for adjustment.

To summarize, our method outperforms existing approaches, achieving significant improvements in both planimetric and vertical accuracy. Utilizing matching confidence information enhances the robustness of the combined adjustment process.

D. Time Performance Analysis

This study conducted experiments across five representative regions, including three small regions (Baotou, Chifeng, Songshan) and two large regions (Hubei, Jiangxi). The specific information for each region is shown in Table I. Hubei and Jiangxi are large-scale areas with significantly more data volume compared to the small regions. These experiments were conducted on a machine with 16 GB RAM, a 1 TB SSD, and a 20-core Intel i7-13709KF processor.

As shown in Table VI, our algorithm completes the combined bundle adjustment for provincial-scale data efficiently within a day on a standard machine. The total processing time for Hubei is 925.2 min (15.4 h), while Jiangxi takes 1176.0 min (19.6 h), demonstrated the method's feasibility for large-scale remote sensing mapping.

DSM generation, due to its dense features, is the most time-consuming step. Without our optimization, generating the full DSM for matching with ICESat-2 data would take 4932.6 min (82.2 h) for Hubei and 7424.3 min (123.7 h) for Jiangxi. However, by generating DSMs only for the regions covered by laser tracks, as explained in Section II-A-2, we reduced the DSM generation time by 77% to 90%. This reduction in time was achieved without compromising the accuracy of the bundle adjustment, ensuring the efficiency of the combined processing of ICESat-2 and optical satellite data for large regions.

When analyzing time consumption from small to large regions, we observed a nearly linear increase across all processing stages. For smaller regions, such as Baotou and Chifeng, local DSM generation took between 7.5 and 9.8 min (for 2 images). In contrast, for larger regions like Hubei and Jiangxi, the process required 571.7 min (297 images) and 679.4 min (255 images), respectively. This nearly linear growth in processing time demonstrated the algorithm's scalability to larger datasets and its potential for global-scale applications.

IV. Conclusion

In this study, we present a robust matching and weighted combined adjustment method that leverages ICESat-2 GLAS data to enhance the geometric positioning accuracy of optical satellites in large survey areas. Our approach accounts for the time-variant characteristics of both ICESat-2 and optical images. We validated the performance of our matching algorithm through extensive experiments. Additionally, we introduced a confidence-based weighting strategy in the combined adjustment process. Our method achieved a horizontal accuracy of 4.3 m and a vertical accuracy of 1.7 m across different landforms in Hubei and Jiangxi, China. These findings underscore the effectiveness and practicality of our method.

While the method has shown promising results in Hubei and Jiangxi, its applicability to global-scale mapping, especially in extreme terrains like glacier-covered regions or deep canyons. Such regions often have complex topographies and significant climate variability, leading to temporal discrepancies between optical satellite imagery and laser altimetry data, which may result in matching errors. Future research should expand the scope of experimentation to include these challenging environments, verifying the method's robustness and generalizability. Furthermore, integrating multi-source satellite data, such as SAR, could further improve the accuracy of combined mapping in complex terrains and dynamic climate conditions.

References

[1] D. Li, "A review of high resolution optical satellite surveying and mapping technology," *Spacecraft Recovery Remote Sens.*, vol. 41, no. 2, pp. 1–11, 2020.

[2] N. Jiao et al., "A generic framework for improving the geopositioning accuracy of multi-source optical and SAR imagery," *ISPRS J. Photogrammetry Remote Sens.*, vol. 169, pp. 377–388, 2020.

[3] P. Zhou et al., "SRTM-assisted block adjustment for stereo pushbroom imagery," *Photogrammetric Rec.*, vol. 33, no. 161, pp. 49–65, 2018.

[4] B. E. Schutz et al., "Overview of the ICESat mission," *Geophysical Res. Lett.*, vol. 32, no. 21, 2005, Art. no. L21S01.

[5] T. Markus et al., "The ice, cloud, and land elevation satellite-2 (ICESat-2): Science requirements, concept, and implementation," *Remote Sens. Environ.*, vol. 190, pp. 260–273, 2017.

[6] X. Tian and J. Shan, "Comprehensive evaluation of the ICESat-2 ATL08 terrain product," *IEEE Trans. Geosci. Remote Sens.*, vol. 59, no. 10, pp. 8195–8209, Oct. 2021.

[7] B. Li et al., "A method of extracting high-accuracy elevation control points from ICESat-2 altimetry data," *Photogrammetric Eng. Remote Sens.*, vol. 87, no. 11, pp. 821–830, 2021.

[8] J. Yu et al., "Accuracy assessment of ICESat-2 ground elevation and canopy height estimates in mangroves," *IEEE Geosci. Remote Sens. Lett.*, vol. 19, 2022, Art. no. 2501405, doi: 10.1109/LGRS.2021.3107440.

[9] M. Gao et al., "Assessment of ICESat-2's horizontal accuracy using an iterative matching method based on high-accuracy terrains," *Remote Sens.*, vol. 15, no. 9, Art. no. 2236, 2023.

[10] T. Schenk, B. Csatho, and T. Neumann, "Assessment of ICESat-2's horizontal accuracy using precisely surveyed terrains in McMurdo Dry Valleys, Antarctica," *IEEE Trans. Geosci. Remote Sens.*, vol. 60, 2022, Art. no. 4303811.

[11] X. Tang et al., "Verification of ZY-3 satellite imagery geometric accuracy without ground control points," *IEEE Geosci. Remote Sens. Lett.*, vol. 12, no. 10, pp. 2100–2104, Oct. 2015.

[12] X. Tang et al., "Overview of the GF-7 laser altimeter system mission," *Earth Space Sci.*, vol. 7, no. 1, 2020, Art. no. e2019EA000777.

[13] D. Qv et al., "ZY-3 block adjustment and DSM vertical accuracy evaluation supported by ICESat/GLAS laser points," in *Proc. 7th Symp. Novel Photoelectron. Detection Technol. Appl.*, 2021, vol. 11763, pp. 1373–1378.

[14] P. Zhou, X. Tang, D. Li, and X. Wang, "Combined block adjustment of stereo imagery and laser altimetry points of the ZY3-03 satellite," *IEEE Geosci. Remote Sens. Lett.*, vol. 19, 2022, Art. no. 6506705.

[15] G. Y. Li et al., "Improve the ZY-3 height accuracy using ICESat/GLAS laser altimeter data," in *Proc. 23rd Congr. Int. Soc. Photogrammetry Remote Sens.*, Jul. 2016, pp. 37–42.

[16] G. Y. Li et al., "ZY-3 block adjustment supported by GLAS laser altimetry data," *Photogrammetric Rec.*, vol. 31, no. 153, pp. 88–107, 2016.

[17] C. Liu, X. Tang, H. Zhang, G. Li, X. Wang, and F. Li, "Geopositioning improvement of ZY-3 satellite imagery integrating GF-7 laser altimetry data," *IEEE Geosci. Remote Sens. Lett.*, vol. 19, Dec. 2022, Art. no. 6503805, doi: 10.1109/LGRS.2021.3136389.

[18] J. Y. Chen et al., "Registration and combined adjustment for the laser altimetry data and high-resolution optical stereo images of the GF-7 satellite," *Remote Sens.*, vol. 14, no. 7, Art. no. 1652, 2022.

[19] G. Li et al., "Integration of ZY3-02 satellite laser altimetry data and stereo images for high-accuracy mapping," *Photogrammetric Eng. Remote Sens.*, vol. 84, no. 9, pp. 569–578, 2018.

[20] W. Lian et al., "Extraction of high-accuracy control points using ICESat-2 ATL03 in urban areas," *Int. J. Appl. Earth Observation Geoinf.*, vol. 115, 2022, Art. no. 103116.

[21] M. Wang, Y. Wei, and Y. Pi, "Geometric positioning integrating optical satellite stereo imagery and a global database of ICESat-2 laser control points: A framework and key technologies," *Geo-Spatial Inf. Sci.*, vol. 26, pp. 206–217, 2023.

[22] S. J. Liu et al., "An alternative approach for registration of high-resolution satellite optical imagery and ICESat laser altimetry data," *Sensors*, vol. 16, no. 12, 2016, Art. no. 2047.

[23] X. L. Zhang et al., "Satellite remote sensing image stereoscopic positioning accuracy promotion based on joint block adjustment with ICESat-2 laser altimetry data," *IEEE Access*, vol. 9, pp. 113362–113376, 2021.

[24] X. Huang, G. Mei, and J. Zhang, "Cross-source point cloud registration: Challenges, progress and prospects," *Neurocomputing*, vol. 548, 2023, Art. no. 126383.

[25] X. Huang et al., "A comprehensive survey on point cloud registration," 2021, *arXiv:2103.02690*.

[26] F. Wang and Z. Zhao, "A survey of iterative closest point algorithm," in *Proc. Chin. Automat. Congr.*, 2017, pp. 4395–4399.

[27] H. M. Le et al., "SDRSAC: Semidefinite-based randomized approach for robust point cloud registration without correspondences," in *Proc. IEEE/CVF Conf. Comput. Vis. Pattern Recognit.*, 2019, pp. 124–133.

[28] H. Yang, J. Shi, and L. Carlone, "TEASER: Fast and certifiable point cloud registration," *IEEE Trans. Robot.*, vol. 37, no. 2, pp. 314–333, Apr. 2021.
[29] J. Zhang, Y. Yao, and B. Deng, "Fast and robust iterative closest point," *IEEE Trans. Pattern Anal. Mach. Intell.*, vol. 44, no. 7, pp. 3450–3466, Jul. 2022.
[30] A. Zeng, S. Song, M. Nießner, M. Fisher, J. Xiao, and T. Funkhouser, "3DMatch: Learning local geometric descriptors from RGB-D reconstructions," in *Proc. IEEE Conf. Comput. Vis. Pattern Recognit.*, 2017, pp. 1802–1811.
[31] H. Deng, T. Birdal, and S. Ilic, "PPFNet: Global context aware local features for robust 3D point matching," in *Proc. IEEE Conf. Comput. Vis. Pattern Recognit.*, 2018, pp. 195–205.
[32] Z. Gojcic, C. Zhou, J. D. Wegner, and A. Wieser, "The perfect match: 3D point cloud matching with smoothed densities," in *Proc. IEEE/CVF Conf. Comput. Vis. Pattern Recognit.*, 2019, pp. 5545–5554.
[33] Z. Qin et al., "GeoTransformer: Fast and robust point cloud registration with geometric transformer," *IEEE Trans. Pattern Anal. Mach. Intell.*, vol. 45, no. 8, pp. 9806–9821, Aug. 2023.
[34] W. Lu, G. Wan, Y. Zhou, X. Fu, P. Yuan, and S. Song, "DeepVCP: An end-to-end deep neural network for point cloud registration," in *Proc. IEEE/CVF Int. Conf. Comput. Vis.*, 2019, pp. 12–21.
[35] J. Li, Q. Hu, and M. Ai, "Point cloud registration based on one-point RANSAC and scale-annealing biweight estimation," *IEEE Trans. Geosci. Remote Sens.*, vol. 59, no. 11, pp. 9716–9729, Nov. 2021.
[36] X. Huang, L. Fan, Q. Wu, J. Zhang, and C. Yuan, "Fast registration for cross-source point clouds by using weak regional affinity and pixel-wise refinement," in *Proc. IEEE Int. Conf. Multimedia Expo*, 2019, pp. 1552–1557.
[37] J. Ye et al., "High-precision digital surface model extraction from satellite stereo images fused with ICESat-2 data," *Remote Sens.*, vol. 14, no. 1, 2022, Art. no. 104.
[38] S. Zou et al., "ICESat-2 laser altimetry data-guided high-accuracy positioning of satellite stereo images," *ISPRS Ann. Photogrammetry, Remote Sens. Spatial Inf. Sci.*, vol. V-1-2022, pp. 41–48, 2022.
[39] P. Gläser et al., "Co-registration of laser altimeter tracks with digital terrain models and applications in planetary science," *Planet. Space Sci.*, vol. 89, pp. 111–117, 2013.
[40] J. Gong et al., "A review of multi-temporal remote sensing data change detection algorithms," *Int. Arch. Photogramm. Remote Sens. Spatial Inf. Sci.*, vol. XXXVII, Part B7, pp. 757–762, 2008.
[41] PhoREAL, "Photon research and engineering analysis library for ICESat-2 data analysis," Version 3.30, GitHub Repository, Feb. 2022. [Online]. Available: https://github.com/icesat-2UT/PhoREAL
[42] L. Cenci, M. Galli, G. Palumbo, L. Sapia, C. Santella, and C. Albinet, "Describing the quality assessment workflow designed for DEM products distributed via the Copernicus Programme. Case study: The absolute vertical accuracy of the copernicus DEM dataset in Spain," in *Proc. IEEE Int. Geosci. Remote Sens. Symp.*, 2021, pp. 6143–614.
[43] G. Facciolo, C. De Franchis, and E. Meinhardt-Llopis, "Automatic 3D reconstruction from multi-date satellite images," in *Proc. IEEE Conf. Comput. Vis. Pattern Recognit. Workshops*, 2017, pp. 57–66.
[44] H. Li et al., "Global DEMs vary from one to another: An evaluation of newly released Copernicus, NASA and AW3D30 DEM on selected terrains of China using ICESat-2 altimetry data," *Int. J. Digit. Earth*, vol. 15, no. 1, pp. 1149–1168, 2022.
[45] Cohen, Y. Huang et al., "Pearson correlation coefficient," in *Proc. Noise Reduction Speech Process.*, 2009, pp. 1–4.
[46] T. Kariya and H. Kurata, *Generalized Least Squares*. Hoboken, NJ, USA: Wiley, 2004.
[47] M. R. Shortis, T. A. Clarke, and T. Short, "Comparison of some techniques for the subpixel location of discrete target images," in *Proc. Videometrics III*, 1994, vol. 2350, pp. 239–250.
[48] S. M. Anthony and S. Granick, "Image analysis with rapid and accurate two-dimensional gaussian fitting," *Langmuir*, vol. 25, no. 14, pp. 8152–8160, 2009.
[49] C. V. Tao and Y. Hu, "A comprehensive study of the rational function model for photogrammetric processing," *Photogrammetric Eng. Remote Sens.*, vol. 67, no. 12, pp. 1347–1358, 2001.
[50] Grodecki and G. Dial, "Block adjustment of high-resolution satellite images described by rational polynomials," *Photogrammetric Eng. Remote Sens.*, vol. 69, no. 1, pp. 59–68, 2003.
[51] P. J. Bickel, "One-step Huber estimates in the linear model," *J. Amer. Stat. Assoc.*, vol. 70, no. 350, pp. 428–434, 1975.
[52] D. G. Lowe, "Distinctive image features from scale-invariant keypoints," *Int. J. Comput. Vis.*, vol. 60, no. 2, pp. 91–110, 2004.
[53] G. Zhang et al., "Combined block adjustment for optical satellite stereo imagery assisted by spaceborne SAR and laser altimetry data," *Remote Sens.*, vol. 13, no. 16, 2021, Art. no. 3062.
[54] Y.-H. Jiang, S. Wei, M. Xu, G. Zhang, and J.-Y. Wang, "Combined adjustment pipeline for improved global geopositioning accuracy of optical satellite imagery with the aid of SAR and GLAS," *IEEE J. Sel. Topics Appl. Earth Observ. Remote Sens.*, vol. 15, pp. 5076–5085, May 2022, doi: 10.1109/JSTARS.2022.3183594.
[55] Y. Jie, S. Li, Q. Guo, S. Zhou, P. Zhao, and Y. Ma, "Stereo imagery adjustment constrained by building boundary points from ICESat-2," *IEEE Geosci. Remote Sens. Lett.*, vol. 21, May 2024, Art. no. 6501005, doi: 10.1109/LGRS.2024.3399050.
[56] Y. Ruan, G. Cai, and Y. Xue, "Optimization of urban elevation accuracy by combining laser altimetry and stereoscopic imaging," in *Proc. IEEE Int. Geosci. Remote Sens. Symp.*, 2023, pp. 3686–3689.
[57] X Zhang et al., "A two-step block adjustment method for DSM accuracy improvement with elevation control of ICESat-2 Data," *Remote Sens.*, vol. 14, no. 18, 2022, Art. no. 4455.
[58] R. Zhou et al., "Robust co-registration of external laser altimetry points and stereo images," *Sensors Mater.*, vol. 35, pp. 975–987, 2023.

Shaodong Wei received the M.S. degree in automation from the Nanjing University of Aeronautics and Astronautics, Nanjing, China, in 2021. He is currently working toward the Ph.D. degree in photogrammetry and remote sensing from the State Key Laboratory of Information Engineering in Surveying, Mapping, and Remote Sensing, Wuhan University, Wuhan, China.

His research interests include combined processing of satellite multisource data and 3-D modeling of satellite.

Yonghua Jiang received the B.S. and Ph.D. degrees in remote sensing science and technique from the School of Remote Sensing and Information Engineering, Wuhan University, Wuhan, China, in 2010 and 2015, respectively.

Since 2015, he has been with the School of Remote Sensing and Information Engineering, Wuhan University, where he became a Professor in 2023. His research interests include geometry processing of spaceborne optical imagery.

Bin Du received the B.Eng. degreee in surveying and mapping engineering from Wuhan University, Wuhan, China, in 2008.

He is currently a Senior Engineer with the Inner Mongolia Surveying and Mapping Geographic Information Center, Hohhot, China. His research interests include remote sensing data processing and application system development. Mr. Du was the recipient of multiple awards, including the Chinese Society for Geodesy Science and Technology Progress Award. He has led several key regional projects.

MeiLin Tan received the B.S. degree in remote sensing science and technology and the M.S. degree in surveying and mapping engineering from Wuhan University, Wuhan, China, in 2010 and 2018, respectively.

He is currently an Engineer with Inner Mongolia Autonomous Region Surveying and Mapping Geographic Information Center, Hohhot, China.

Miaozhong Xu received the B.S. degree in surveying and mapping engineering from the Wuhan Technical University of Surveying and Mapping, Wuhan, China, in 1989, and the Ph.D. degree in photogrammetry and remote sensing from the State Key Laboratory of Information Engineering in Surveying, Mapping, and Remote Sensing, Wuhan University, Wuhan, in 2004.

He is currently a Professor with the State Key Laboratory of Information Engineering in Surveying, Mapping, and Remote Sensing, Wuhan University. His research interests include high-resolution image processing, photogrammetry, and cartography.

Weiqi Lian received the bachelor's degree in geographic information science from Zhengzhou University, Zhengzhou, China, in 2018, and the Ph.D. degree in photogrammetry and remote sensing from Wuhan University, Wuhan, China, in 2023.

She is currently a Lecturer with Information Engineering University, Zhengzhou. Her research interests include spaceborne laser data processing and application.

Guo Zhang (Member, IEEE) received the B.E. and Ph.D. degrees in photogrammetry and remote sensing from the School of Remote Sensing and Information Engineering, Wuhan University, Wuhan, China, in 2000 and 2005, respectively. His Ph.D. dissertation concerned the rectification of high-resolution remote sensing imaging under lack of ground control points.

He has been working with the State Key Laboratory of Information Engineering in Surveying, Mapping and Remote Sensing (LIESMARS), Wuhan University, since 2005, where he became a Professor in 2011. His research interests include space photogrammetry, geometry processing of spaceborne optical/synthetic aperture radar (SAR)/InSAR imagery, altimetry, and high-accuracy image matching.